Direct numerical simulation of shock wave/turbulent boundary layer interaction in a swept compression ramp at Mach 6 ⓔⓟ ✓

Ji Zhang (张吉); Tongbiao Guo (郭同彪); Guanlin Dang (党冠麟); ... et. al

Check for updates

CrossMark

View Online   Export Citation

Articles You May Be Interested In

Response characteristics of impinging shock wave/turbulent boundary layer interaction disturbed by arc plasma energy deposition
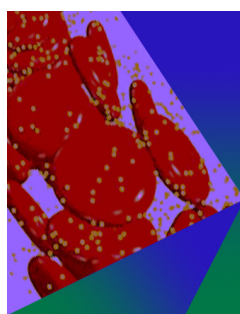
Physics of Fluids (January 2022)

Unsteadiness characterization of shock wave/turbulent boundary layer interaction controlled by high-frequency arc plasma energy deposition

Physics of Fluids (January 2021)

Compressibility effect on interaction of shock wave and turbulent boundary layer

Physics of Fluids (July 2022)

Physics of Fluids

Special Topic: Flow and Forensics

Submit Today!

AIP Publishing

Direct numerical simulation of shock wave/turbulent boundary layer interaction in a swept compression ramp at Mach 6 🔵EP

View Online   Export Citation   CrossMark

Ji Zhang (张吉),[1,2] 🆔 Tongbiao Guo (郭同彪),[1] 🆔 Guanlin Dang (党冠麟),[1,2] 🆔 and Xinliang Li (李新亮)[1,2,a] 🆔

AFFILIATIONS

[1]LHD, Institute of Mechanics, Chinese Academy of Sciences, Beijing 100190, China
[2]School of Engineering Science, University of Chinese Academy of Sciences, Beijing 100049, China

[a]Author to whom correspondence should be addressed: lixl@imech.ac.cn

ABSTRACT

Swept compression ramps widely exist in supersonic/hypersonic vehicles and have become a typical standard model for studying three-dimensional (3D) shock wave/turbulent boundary layer interactions (STBLIs). In this paper, we conduct a direct numerical simulation of swept compression ramp STBLI with a 34° compression angle and a 45° sweep angle at Mach 6 using a heterogeneous parallel finite difference solver. Benefitting from the powerful computing performance of the graphics processing unit, the computational grid number exceeds 5 $\times 10^6$ with the spatiotemporal evolution data of hypersonic 3D STBLI obtained. The results show that the flow of the hypersonic swept compression ramp follows the quasi-conical symmetry. A supersonic crossflow with helical motion appears in the interaction region, and its velocity increases along the spanwise direction. Fluids from the high-energy-density region pass through the bow shock at the head of the main shock and crash into the wall downstream of the reattachment, resulting in the peaks in skin friction and heat flux. The peak friction and heating increase along the spanwise direction because of the spanwise variation in the shock wave inclination. In the interaction region, the unsteadiness is dominated by the mid-frequency motion, whereas the low-frequency large-scale motion is nearly absent. Two reasons for the lack of low-frequency unsteadiness are given: (1) The separation shock is significantly weaker than the reattachment shock and main shock; and (2) because of the supersonic crossflow, the perturbations propagating at the sound speed are not self-sustaining but flow along the r-direction and toward the spanwise boundary.

Published under an exclusive license by AIP Publishing. https://doi.org/10.1063/5.0118578

I. INTRODUCTION

Shock wave/turbulent boundary layer interactions (STBLIs) occur widely in the internal and external flow of supersonic/hypersonic vehicles such as scramjets and rudder surfaces. STBLIs have attracted a lot of research attention in the past decades.[1] In the flow, the increase in pressure caused by the shock usually leads to the separation of the boundary layer and the formation of separation shock and reattachment shock. STBLI is unstable, and its unsteadiness is characterized by a wide range of frequency.[2] Among the unsteady motions with various frequencies, the low-frequency, large-scale motion of the separation shock foot is the focus of attention. Its oscillation frequency is usually one to two orders of magnitude lower than the characteristic frequency of the upstream turbulent boundary layer. In supersonic flight, low-frequency unsteadiness is dangerous, especially when the oscillation frequency is close to the natural frequency of the aircraft, which can cause resonance and fatigue of the aerostructure. In high-speed flight, peak heating near the reattachment is also a severe problem and can lead to heavy thermal loading on the aircraft surface.

In the last century, experiments were the primary means of studying STBLIs. In 1991, Erengil and Dolling[3] performed an experimental study on a Mach 5 compression ramp and verified the existence of low-frequency unsteadiness at the position of the separation shock foot under hypersonic conditions. With the rapid development of computer technology, large-eddy simulation (LES) and direct numerical simulation (DNS) have become important means of studying STBLIs. Pirozzoli and Grasso[4,5] and Wu and Martin[6–8] have achieved great success in DNS. Pasquariello *et al.*[9] used LES to study impinging shock interactions and the relationship between low-frequency unsteadiness and Görtler-like vortices. Recently, Priebe and Martin[10] conducted a DNS of a hypersonic Mach 7 compression ramp STBLI.

It is worth emphasizing that most previous studies on STBLIs have focused on two-dimensional (2D) STBLIs, such as impinging shock interactions and compression ramp interactions. Compared to 2D interactions, there is much less research on three-dimensional (3D) interactions, especially using numerical simulations. The shock generator of 3D STBLIs can cause spanwise inhomogeneity, resulting in obvious differences from 2D interactions.

In the early stage of research on 3D interactions, the experimental results of Settles and Teng[11] showed two characteristic flow states in 3D STBLIs: cylindrical and conical. Afterward, Settles *et al.*[12,13] conducted experiments on three shock generators: sharp fins, semicones, and swept compression corners. Their work revealed conical free interaction and quasi-conical symmetry in 3D STBLIs. The perfect conical symmetry means that there is a virtual conical origin (VCO) in the flow field, and if a spherical coordinate system is established with the VCO as the coordinate origin, the flow characteristics in a specific radius direction are similar. However, the actual flow does not entirely follow the perfect conical symmetry, especially in a region with a small radius. This imperfect symmetry is called quasi-conical symmetry. Erengil and Dolling[14] conducted an experimental study on Mach 5 swept compression ramp interactions. They found that the flow followed the cylindrical symmetry in the case of a small sweep angle but the quasi-conical symmetry in the case of a large sweep angle. The former showed low-frequency, large-scale pulsation at the location of the separated shock wave, whereas the latter showed high-frequency, small-scale pulsation. Vanstone *et al.*[15–17] studied the mechanism of unsteadiness and certain limiting cases of the scaling laws through an experiment on a Mach 2 swept compression ramp interaction. In recent years, the numerical study of 3D STBLIs has been gradually increasing. Adler and Gaitonde[18,19] studied sharp fins and swept compression corners at Mach 2 using LES and further verified the quasi-conical symmetry. They found that the lack of low-frequency unsteadiness in 3D interactions could be related to the lack of absolute instability. Renzo *et al.*[20] performed DNS of a special impinging shock interaction in which the upstream flow made an angle with respect to the direction normal to the nominal shock impingement line. It should be noted that they called it "two-dimensional, three-component flow" rather than real 3D interaction flow.

At present, there are a few DNSs of 3D STBLIs, especially for hypersonic flow. The shock wave is much stronger at a high Mach number than at a low Mach number, and so is the heat flux. The difficulty of DNS is that its computational scale is much higher than that of other numerical methods, such as LES. Moreover, simulating 3D interactions requires a larger spanwise computational domain, which further improves the computational scale of DNS. In addition, flow with a higher Mach number brings a greater challenge to the robustness of the high-precision numerical scheme. Nevertheless, DNS of hypersonic 3D STBLIs is still necessary. DNS has extremely high resolution and fidelity, which helps to deepen understanding of STBLI. With the improved computing power and efficiency of the graphics processing unit (GPU), heterogeneous parallel computing using GPU significantly reduces the computing cost of DNS, which facilitates DNS with billions of grids. Elsen *et al.*[21] used GPU to calculate the flow over a hypersonic vehicle, and the calculation speed was greatly improved compared to the central processing unit (CPU). In recent years, the GPU-accelerated solvers ZEFR,[22] HTR,[23] and STREAmS[24] further demonstrated the powerful computing performance of the GPU.

In this paper, we report a DNS of a hypersonic swept compression ramp STBLI using heterogeneous parallel computing with GPU. In Sec. II, the numerical methods and the verification of computation are introduced, including the heterogeneous parallel programs, numerical schemes, grid settings, and statistical law of the flat-plate turbulent boundary layer. Section III presents the results and discussion, including the 3D flow structure, the mechanism of high skin friction and heat flux, and the low-frequency unsteadiness. This study aims to obtain high-fidelity spatiotemporal evolution data of hypersonic 3D STBLI and reveal some flow phenomena different from 2D STBLI.

II. METHODOLOGY
A. Governing equations

The governing equations solved in this paper are dimensionless 3D compressible Navier–Stokes equations in a curvilinear coordinate system (ξ, η, ζ),

$$\frac{\partial Q}{\partial t} + \frac{\partial (F_c + F_v)}{\partial \xi} + \frac{\partial (G_c + G_v)}{\partial \eta} + \frac{\partial (H_c + H_v)}{\partial \zeta} = 0, \quad (1)$$

where t is the time coordinate; Q represents the conservative variables; F_c, G_c, and H_c represent the convection flux terms in the ξ, η, and ζ directions; and F_v, G_v, and H_v are the corresponding viscous terms. Non-dimensionalization is performed with the unit reference length (1 mm) and the free-stream parameters, including velocity U_∞, density ρ_∞, and temperature T_∞. The expression of each term in Eq. (1) is the same as that in Wu and Martin.[6]

The high-precision finite difference solver OpenCFD-SCU (open computational fluid dynamic code for scientific computation with GPU system) is used for computation.[43] This solver is a heterogeneous parallel version of the finite difference solver OpenCFD-SC (open computational fluid dynamic code for scientific computation). In previous computations and studies,[25–29] the accuracy and reliability of OpenCFD-SC were verified. Some optimization algorithms are used in OpenCFD-SCU, including memory access coalescing, overlapping computation with communication, and self-adaptation of block size, giving full play to the computing advantages of GPU. With the help of the National Supercomputer Center, we tested the performance of OpenCFD-SCU, finding that its computation speed using one GPU can reach hundreds of times that of OpenCFD-SC using one CPU core. The parallel efficiency (weak scalability) of the program can reach about 98.7% on 24 576 GPUs. Considering the comprehensive energy efficiency, OpenCFD-SCU reduces the computing cost by more than 90%, which makes it possible to conduct huge-scale DNS.

The eighth-order central difference scheme is used to compute the viscous terms. The characteristic-based[30] Steger–Warming splitting and the hybrid difference scheme (HDS) are used to compute the convection terms. The HDS includes the sixth-order monotonicity-preserving optimized scheme (OMP6)[31] and the seventh-order weighted essentially non-oscillatory scheme (WENO7).[32] The former has lower dissipation, whereas the latter has better robustness. The pressure gradient is used as the shock recognizer of the HDS to choose the appropriate scheme. OMP6 and WENO7 are adopted for the low-pressure-gradient (smooth) and high-pressure-gradient (non-smooth) regions, respectively. Time integration is performed with the third-order total-variation-diminishing Runge–Kutta method.
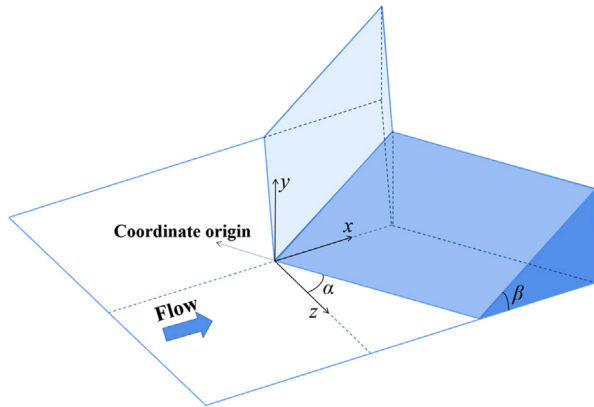
FIG. 1. Principal configuration of the symmetrical swept compression ramp.

B. Computational parameters and mesh

The computational configuration is a symmetrical swept compression ramp with the sweep angle $\alpha = 45°$ and the compression angle $\beta = 34°$, as shown in Fig. 1. The origin of the coordinate system is located at the intersection of the symmetry plane and the corner line. As shown in Fig. 2, the shaded area is the core zone of the simulation where the spanwise spacing of the grid is small and uniform, whereas the other area is the grid stretching area (buffer zone) where the grid resolution is relatively low. In the corner region of the core zone, the mesh is further densified to ensure the computational accuracy of the interaction, as shown in Fig. 3. The spanwise domain of the core zone ranges from $z = -10$ mm to $z = 60$ mm to ensure accuracy near the symmetry plane and reduce the overall computation. The height of the normal domain is 55 mm. The length of the streamwise domain L_x changes with the spanwise position (i.e., $L_x = |z| + 439.7$ mm), so the maximum of L_x is 499.7 mm when $z = 60$ mm, with the corresponding streamwise domain ranging from $x = -390$ mm to $x = 109.7$ mm. The verification and analysis of the computational results in this paper are for the core zone only.

The boundary conditions are as follows: The profile of the flat-plate laminar boundary layer is applied at the inlet, and the thickness of the boundary layer is about 3.9 mm; the isothermal no-slip boundary condition is applied on the wall; and the non-reflective boundary

condition and buffer zone are applied at the outlet, upper boundary, and spanwise boundary to eliminate the influence of perturbation wave reflection on the simulation of the core zone. In addition, multi-frequency sine wave disturbance[4] is applied in the region ranging from $x = -370$ mm to $x = -350$ mm to stimulate the by-pass transition of the boundary layer and enable the flow to reach a state of fully developed turbulence in front of the interaction area.

The free-stream parameters are as follows: Mach number $M_\infty = 6$, unit Reynolds number $Re = 10\,000$/mm, specific heat ratio $\gamma = 1.4$, Prandtl number $Pr = 0.70$, static temperature $T_\infty = 79$ K, and wall temperature $T_w = 294$ K. The recovery temperature $T_r = T_\infty\left(1 + r(\gamma - 1)M_\infty^2/2\right) = 585\,K > T_w$, where r is the temperature recovery coefficient and is taken to be 0.89, so the given wall is cold.

Two sets of grids are used in the simulation, as shown in Table I, where Δy_w^+ and Δy_e^+ represent the resolution at the wall and outer edge of the boundary layer, respectively. The numbers of grid points of Mesh 1 and Mesh 2 are about 2.06×10^9 and 5.51×10^9, respectively. The normal heights of the first grid point off the wall of Mesh 1 and Mesh 2 are 0.01 and 0.008 mm, respectively, and the corresponding dimensionless time integration steps are 0.008 and 0.006, respectively.

C. Verification of results

Figure 4 shows the time-averaged wall pressure p_w, skin friction coefficient $C_f = \tau_w/\left(0.5\rho_\infty U_\infty^2\right)$, and Stanton number St $= q_w/\left[\rho_\infty U_\infty(h_{aw} - h_w)\right]$ of Mesh 1 and Mesh 2 in the planes of $z = 15, 30, 45$ mm, where τ_w is the wall shear stress; q_w is the heat transfer rate on the wall; and h_w and h_{aw} are the enthalpy on the wall and adiabatic wall, respectively. The simulation results for the wall pressure in Mesh 1 and Mesh 2 are virtually identical, and the results for skin friction and heat flux are basically the same near the corner when the grid number increases from 2.06×10^9 to 5.51×10^9. Although the peaks in the skin friction and heat flux of Mesh 1 are 7%–10% lower than in Mesh 2, the peak positions of Mesh 1 and Mesh 2 are almost identical.

Figure 5 shows the distribution of the instantaneous skin friction coefficient. E1 is located in the fully developed turbulent boundary layer, where the banded structure of wall turbulence is apparent. E1 is selected as the reference point, and its coordinates (x, y, z) are $(-16.7, 0, 30)$ mm. The turbulent boundary layer parameters at E1 are given in Table II, where δ, δ^*, δ_θ, and H are the boundary layer thickness,
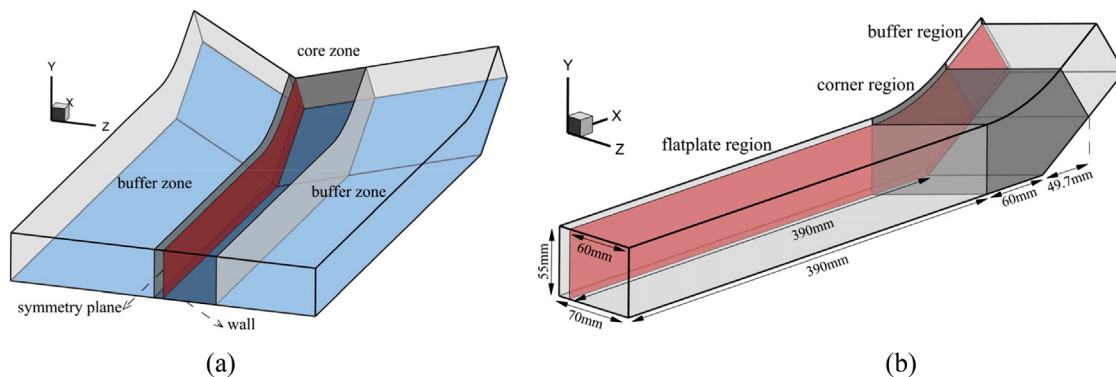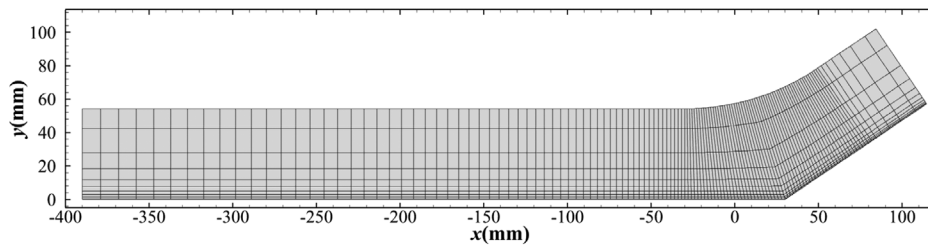
FIG. 2. Computational domain of the symmetrical swept compression ramp. (a) The whole and (b) the core zone.

FIG. 3. Mesh distribution in the x–y plane of $z = 30$ mm. The mesh is plotted every 30 points in the x and y directions.

TABLE I. Grid number and resolution.

Mesh	$N_x \times N_y \times N_z$	$N_x \times N_y \times N_z$ of corner region	Δx^+, $(\Delta y_w^+, \Delta y_e^+)$, Δz^+ in corner region
Mesh 1	$3800 \times 320 \times 1690$	$1800 \times 320 \times 1400$	2.92, (0.44, 5.28), 2.19
Mesh 2	$4740 \times 480 \times 2420$	$2700 \times 480 \times 2100$	1.94, (0.35, 3.53), 1.46

displacement thickness, momentum thickness, and shape factor, respectively. In addition, three x–y planes ($z = 15$, 30, and 45 mm) are selected to analyze the flow characteristics varying along the spanwise direction.

Figure 6(a) shows the mean velocity profile at E1, where U_{VD}^+ is the van Driest transformed mean streamwise velocity and defined as[33]

$$U_{VD}^+ = \int_0^{u^+} \sqrt{\overline{\rho}/\overline{\rho}_w} \, du^+. \qquad (2)$$

The mean velocity profile follows the linear distribution at the viscous sublayer and the logarithmic distribution at the log-law layer. Because of the wall temperature effect,[10,33] the intercept of the log-law is 5.7, higher than that of the incompressible turbulent boundary layer.

In the following analyses, the fluctuation from the Reynolds averaging operation for the general variable ψ is defined as $\psi' = \psi - \overline{\psi}$, where $\overline{\psi}$ is the Reynolds average of ψ. The following transformations[34] are introduced to compare the velocity fluctuations with those in the incompressible turbulent boundary layer:

$$u_i^* = \frac{\sqrt{\overline{\rho}/\overline{\rho}_w}}{u_\tau}\sqrt{\overline{u_i'^2}}, \quad (u_iu_j)^* = \frac{\overline{\rho}/\overline{\rho}_w}{u_\tau^2}\overline{u_i'u_j'}, \qquad (3)$$

where ρ_w is the density on the wall and u_τ is the friction velocity. Figure 6(b) shows the velocity fluctuations at E1, which are basically consistent with the simulations and experimental results of others.[34–38] In addition, the results show that obvious anisotropy exists near the wall.

III. FLOW STRUCTURE

A. Quasi-conical symmetry

Figure 4 shows that there is no region with negative streamwise velocity ($C_f < 0$) near the wall in the plane of $z = 30$ mm. In 2D STBLIs, the area with negative streamwise velocity is usually defined as the separation region, which is unsuitable for 3D interactions. The critical point theory[39] can be used to describe separation and reattachment: Near the separation line, the streamlines converge toward the separation line; near the reattachment line, the streamlines diverge from the reattachment line. Figure 7 shows the separation and

reattachment lines determined by the near-wall streamlines. It should be noted that the black lines in Fig. 7 are not the real streamlines but the projection lines of the near-wall streamlines on the wall. The extension lines of the separation line, reattachment line, and corner line approximately intersect near the VCO, which indicates that the mean flow structure follows the quasi-conical symmetry. A spherical coordinate system (r, θ, φ) is established with the VCO as the coordinate origin. The coordinates (x, y, z) of the VCO are $(-15.8, 0, -15.8)$ mm, as shown in Fig. 7. In this coordinate system, r is the displacement from the origin to point P, θ is the zenith angle between the line from the origin to P (line VCO-P) and the positive y-axis, and φ is the azimuth between the projection line of the line VCO-P in the x–y plane and the positive z axis. The separation line and reattachment line are in the planes of $\varphi = 32.4°$ and $\varphi = 51.2°$, respectively.

In the region with small displacement from the VCO, the separation line and reattachment line are bow-shaped, whereas farther from the VCO, the bow feature is gradually replaced by the linear feature. In other words, where the radius is small, the flow is not conical self-similar, which is why the flow feature is called quasi-conical symmetry rather than conical symmetry. The closer to the VCO, the more easily the flow is affected by external flow that is not conical self-similar. In theory, the flow structure is completely conical self-similar only at infinity, but it is still very convenient to use the spherical coordinate system to describe the flow structure.[18]

Unlike in 2D interactions, there is a flow with noticeable spanwise velocity (a crossflow) in 3D interactions, as shown in Fig. 7. In this paper, the region where the spanwise velocity is greater than the streamwise velocity ($w > u$), shown by the shaded area of Fig. 8, is called the crossflow region. An additional physical meaning of the crossflow region is that the flow deflects more than 45° compared to the incoming flow, which means the component of the local velocity perpendicular to the plane of $\varphi = 45°$ is negative. Figure 9(a) shows the outlines of the crossflow region in different x–y planes. The size of the crossflow region changes linearly with the spanwise position. The starting and ending positions of the crossflow are located at $\varphi = 32.4°$ and $\varphi = 49°$. The starting position of the crossflow is consistent with the separation line, and the ending position is slightly in front of the reattachment line. Therefore, the crossflow region and the separation region correspond.
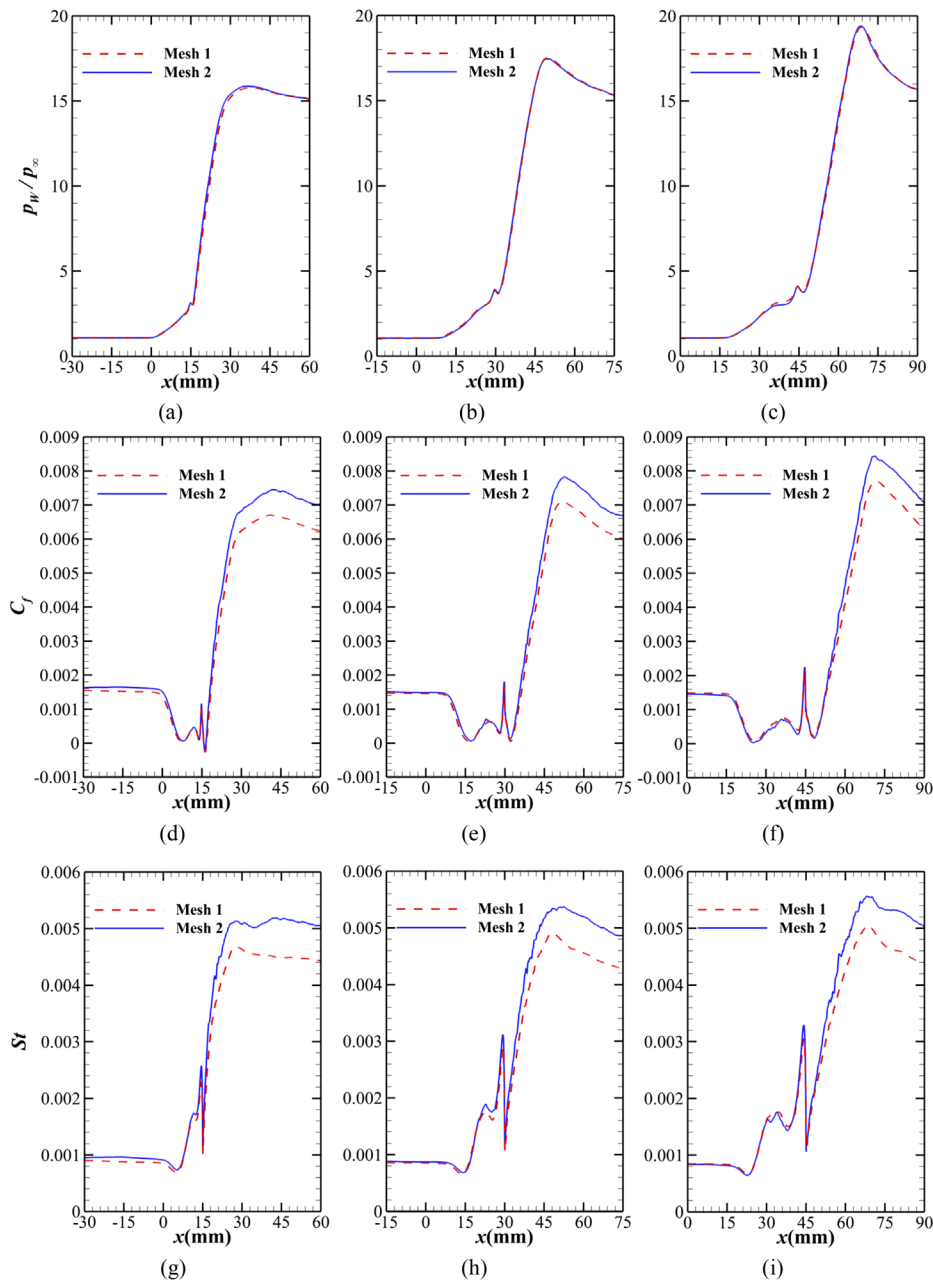
FIG. 4. Distribution of the time-averaged [(a)–(c)] wall pressure, [(d)–(f)] skin friction coefficient, and [(g)–(i)] Stanton number in the x–y planes of [(a), (d), and (g)] $z = 15$ mm, [(b), (e), and (h)] $z = 30$ mm, and [(c), (f), and (i)] $z = 45$ mm in the interaction region.

In the separation region of 2D STBLI, the mean flow structure is a cylindrical vortex. Figure 8 indicates that in 3D STBLI the fluid flows toward the boundary as a helical vortex after entering the quasi-separation region, so the streamlines of the separated flow are not closed. Figure 10(a) shows that at a certain point in the center of the crossflow region, the spanwise velocity reaches the maximum in the plane of $z = 30$ mm. The line connecting each point with the maximum spanwise velocity in each x–y plane is called the centerline of the crossflow region in this paper. According to the quasi-conical symmetry, the centerline approximates to a half-line originating from VCO.

Figure 10(b) further shows the distributions of certain variables on the centerline. In the transition region ($r < 40$ mm), because of the obstruction of the ramp, fluid that initially moves in the streamwise direction deflects rapidly and turns into the crossflow. In the self-similar region ($r > 40$ mm), the crossflow still gradually strengthens along the spanwise direction away from the VCO. The rotation velocity around the center of the crossflow is much less than the spanwise velocity in the separation region. If the fluid rotating is not considered, the crossflow can be regarded as the flow in an expansion tube. Because the velocity of the crossflow is always greater than the local
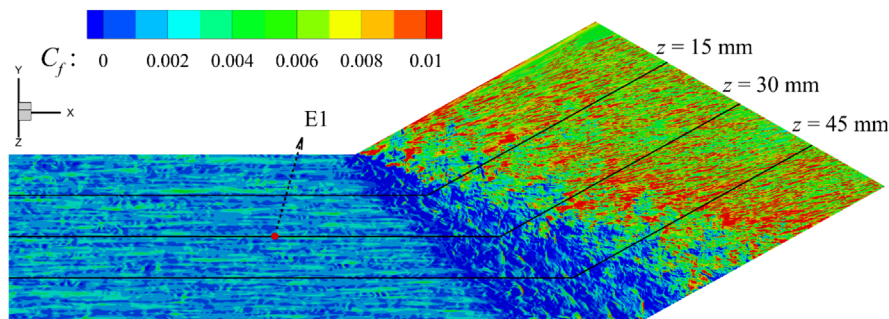
FIG. 5. Instantaneous skin friction coefficient.

TABLE II. Boundary layer parameters at E1.

δ/mm	δ^*/mm	δ_θ/mm	H
8.61	3.33	0.36	9.30

speed of sound, the expansion tube is a supersonic nozzle, and the cross-flow is accelerated. Indeed, the fluid from the flat-plate boundary layer continuously moves into the crossflow region, and the total mass flux of the fluid increases along the spanwise direction, leading to the increasing density, which is different from a general supersonic nozzle. However, it is worth further studying whether the crossflow could be continuously accelerated if the spanwise computational domain was further expanded. If the size of the crossflow region no longer markedly increases along the spanwise direction, the velocity of the crossflow may not rise.

Figure 9(b) shows the outlines of the shock wave in different x–y planes. The separation and reattachment shocks are relatively difficult to display because there are mainly compression wave systems rather than the real shock wave in the separation and reattachment regions. The main shock has 3D characteristics in that as the displacement from the VCO increases, the starting position of the main shock moves downstream, and the shock angle increases. The reason for this phenomenon is that the size of the separation region increases along the spanwise direction, resulting in the reattachment shock wave becoming stronger and moving downstream. In addition, the head of
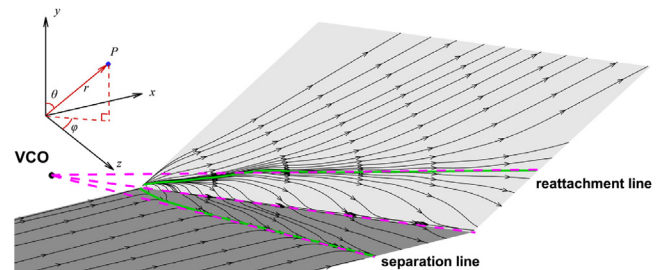

FIG. 7. Streamlines of the mean flow near the wall. The two solid green lines represent the separation line and reattachment line, respectively. In the spherical coordinate system (r, θ, φ), r is the displacement from the origin to point P, θ is the zenith angle between the line from the origin to P (line VCO-P) and the positive y axis, and φ is the azimuth between the projection line of the line VCO-P in the x–y plane and the positive z axis.

the main shock wave is bow-shaped, and the closer to the head of the main shock, the more pronounced the difference in the shock angle at different spanwise positions, whereas in the downstream flow, the shock waves of different x–y planes tend to be parallel.

B. Peak skin friction and heat flux

At present, research on the causes of peak friction and heating in hypersonic STBLI is limited. Because the simulation results for peak
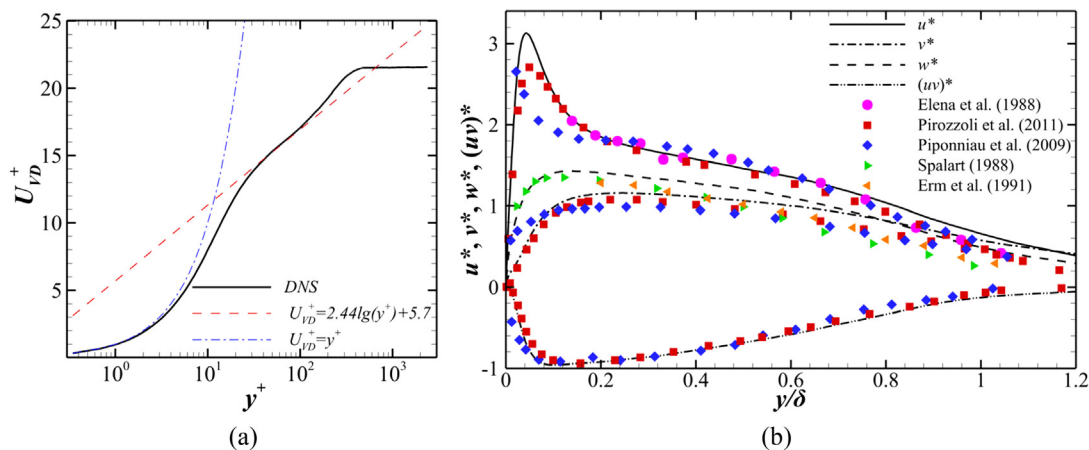

FIG. 6. Profiles of (a) the van Driest transformed mean velocity and (b) velocity fluctuations. The results are taken at E1.
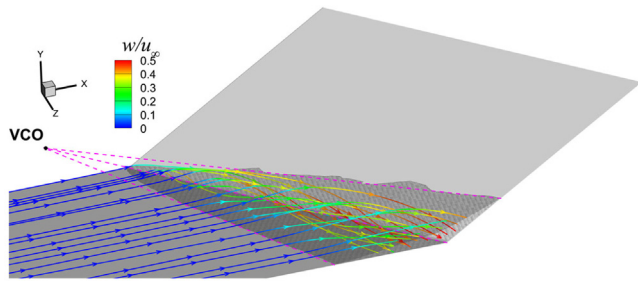
FIG. 8. Streamlines (color-coded by time-averaged spanwise velocity) of the mean flow into the crossflow region.

FIG. 11. Instantaneous density distribution of the interaction region in the plane of $z = 30$ mm.

friction and heating are not fully developed, a qualitative rather than quantitative analysis is done for the peak.

Figure 11 shows the instantaneous density of the interaction region. The shock wave is very close to the wall under hypersonic conditions, so the turbulent boundary layer behind the reattachment is much thinner than before the separation. A high-density flow is formed around the reattachment region, corresponding to the peak
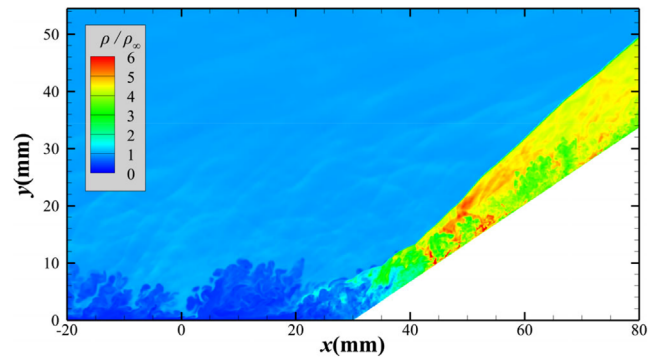
friction and heating in Fig. 4. The Q-criterion[40] is widely used to visualize the vortex structure. Figure 12 shows the shock wave and vortices in the interaction region. In the flat-plate turbulent boundary layer, there are typical streamwise vortices near the wall. After entering the
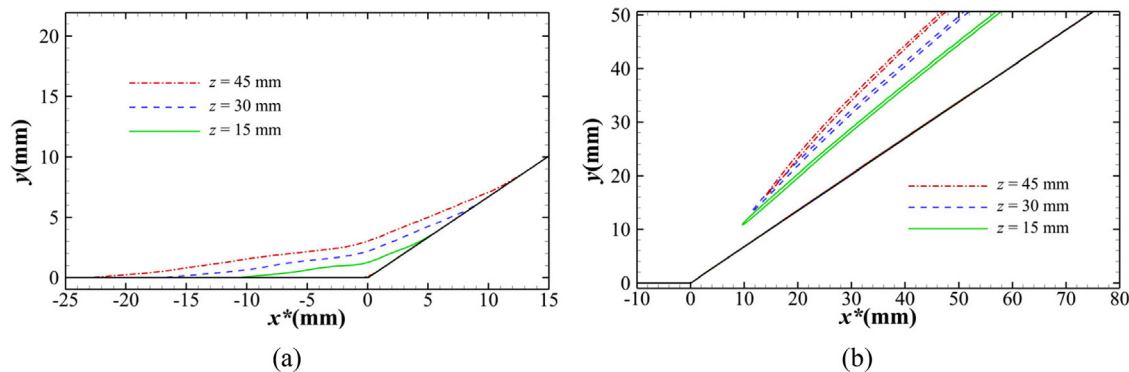

(a)

(b)

FIG. 9. Time-averaged outline of (a) the crossflow region (line $u = w$) and (b) the main shock (contour line $\left|\nabla \rho(x, y)\right|/\rho_\infty = 3$) in the planes of $z = 15$, 30, and 45 mm, where x^* is the abscissa of the coordinate system with the corner as the origin.
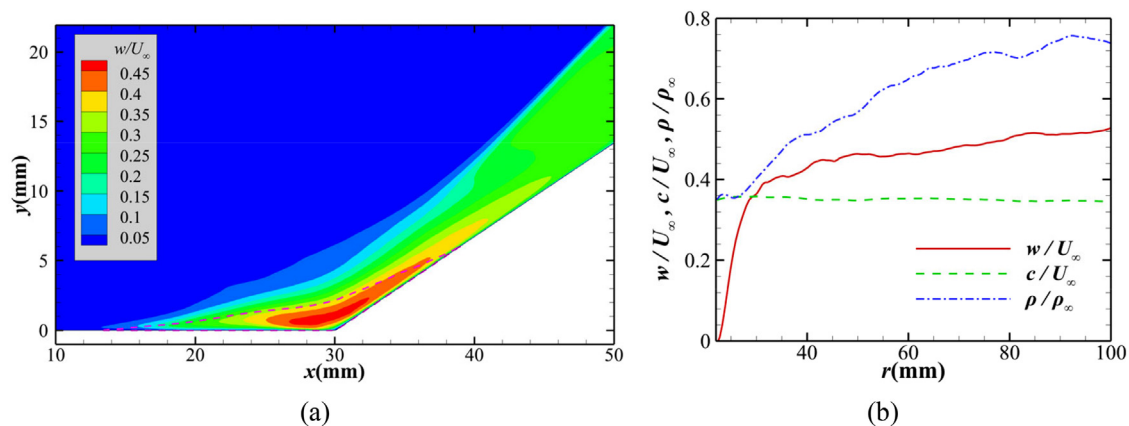

(a)

(b)

FIG. 10. (a) Time-averaged spanwise velocity in the plane of $z = 30$ mm. (b) Time-averaged spanwise velocity, speed of sound c, and density distribution on the centerline of the crossflow region. The pink dashed line is the outline of the crossflow region.
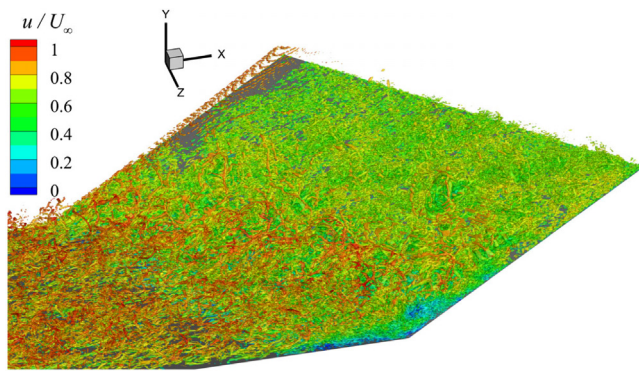
FIG. 12. Instantaneous iso-surfaces of $Q = 0.05$ colored by the streamwise velocity.

interaction region, the vortices near the wall are broken into smaller scale vortices, and some larger scale U-shaped vortices are formed in the region far away from the wall. Downstream of the reattachment, the vortices gradually revert to streamwise vortices with a specific spanwise component. However, compared to the vortices before separation, these vortices are closer to the wall and smaller in scale because of the thinner boundary layer behind the reattachment.

Figure 13 shows the time-averaged wall pressure, skin friction coefficient, and Stanton number. The position of the maximum wall pressure in each x–y plane is distributed in approximately a straight line. For the convenience of analysis, this straight line is called the line of peak pressure in this paper. Similarly, the line of peak skin friction and the line of peak heat flux are obtained. The lines of peak wall pressure, skin friction, and heat flux intersect at the VCO, which further verifies that the flow structure follows the quasi-conical symmetry. Near the reattachment, the iso-lines of physical quantities and the contour of the crossflow region are wavy, which indicates some large-scale structures on the ramp (i.e., Görtler-like vortices).

Figure 14 shows the time-averaged energy density E (including internal energy and kinetic energy), density ρ, and turbulent kinetic energy k in the planes of $z = 30$ mm and $z = 45$ mm. Both E and k are non-dimensionalized with the free-stream parameters in Sec. II. The energy density of the fluid above the separation bubble is significantly higher than that of other fluids in the same streamwise position. The main reason for the formation of the high-energy-density fluid is the increase in density behind the separation, so the distribution of energy density is similar to that of density. In addition, there is a region with strong turbulent kinetic energy between the high-energy-density fluid and the crossflow, as shown in Figs. 14(e) and 14(f). The high-energy-density fluid mainly moves in the streamwise direction and has a higher velocity, whereas the crossflow mainly moves in the spanwise direction and has a lower velocity. Therefore, there is a strong shear layer between the high-energy-density fluid and the crossflow, which significantly increases the turbulent kinetic energy here.

The streamlines in Fig. 13 show that the fluid from the high-energy-density region crashes into the downstream ramp behind the reattachment line. As mentioned before, unlike the oblique shock wave in the inviscid flow, the head of the main shock wave is the bow shock, which means the flow states at different positions behind the main shock wave are distinct. λ, the angle between the local flow
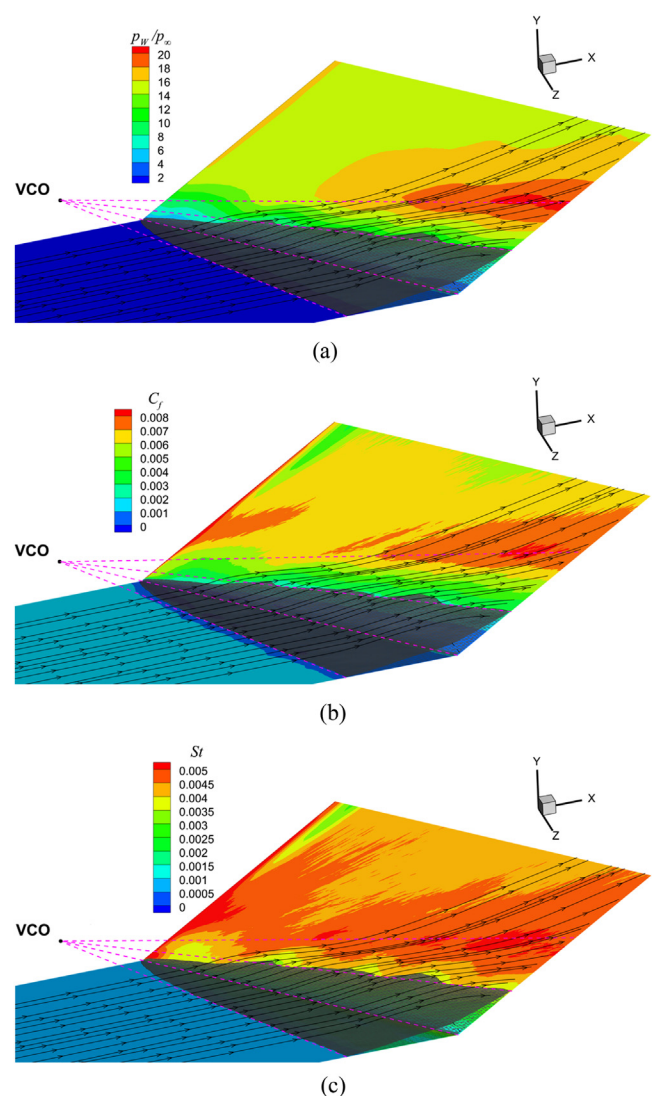

FIG. 13. Time-averaged (a) pressure, (b) coefficients of skin friction, and (c) Stanton number distribution on the wall. The gray area is the crossflow region.

direction and the ramp, is used to quantitatively reflect the impact of the fluid on the wall, as shown in Fig. 15. The fluid passing through the main shock cannot be entirely deflected to the direction parallel to the ramp, especially near the lambda-shock triple-point. Figure 15(b) shows that at a certain height from the wall, there is an extremum λ, and the position of the extremum corresponds to the peak friction and heating. It is worth mentioning that λ near the corner ($x = 45$ mm) is very high, but here is the separated flow whose velocity and density are relatively low, and the impact on the wall is not strong. In the process of the fluid impacting the wall, λ gradually decreases because of the obstruction of the wall. Meanwhile, the fluid is strongly compressed, which leads to an increase in density, pressure, and temperature. In addition, under the impact of the fluid, the boundary layer is relatively thin at the reattachment point, so this becomes a region of
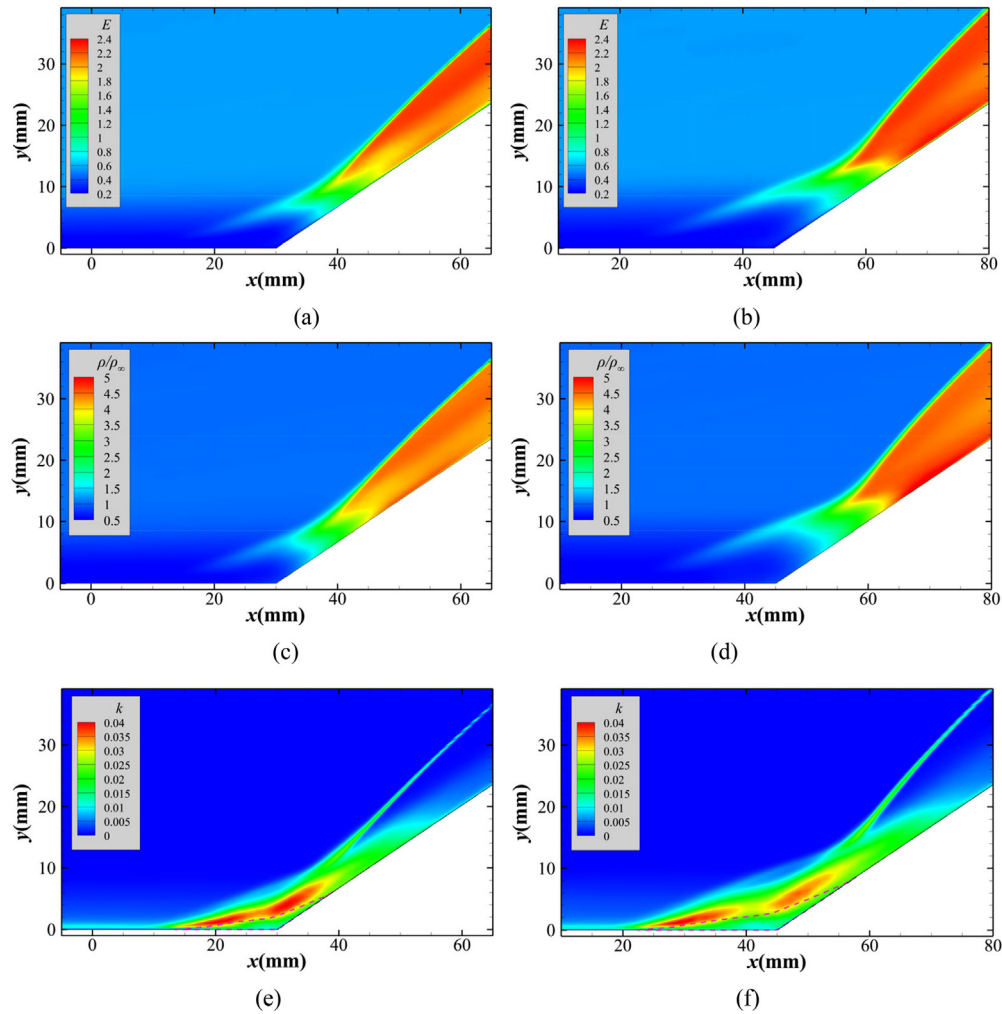
FIG. 14. Time-averaged [(a) and (b)] energy density, [(c) and (d)] density and [(e) and (f)] turbulent kinetic energy in the planes of [(a), (c), and (e)] $z = 30$ mm and [(b), (d), and (f)] $z = 45$ mm. The pink dashed line is the outline of the crossflow region.
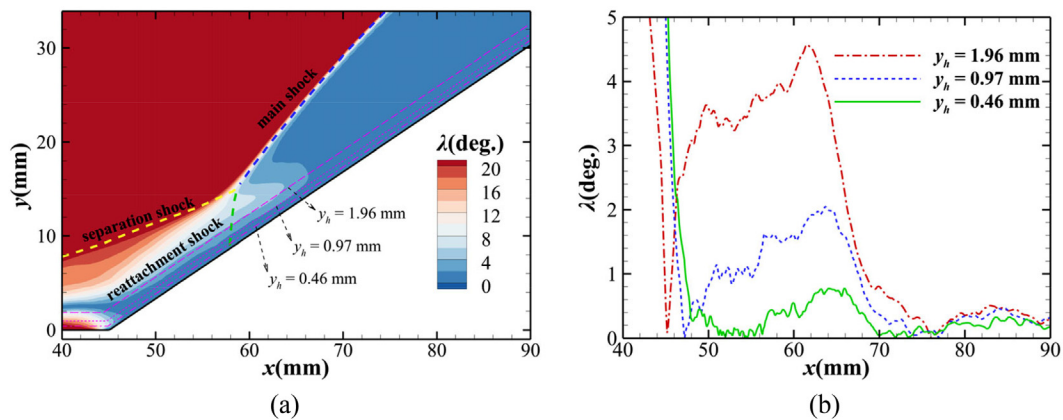

FIG. 15. Time-averaged λ (a) in the plane of $z = 45$ mm and (b) on in-plane lines at different heights y_h from the wall. λ is the angle between the local flow direction and the ramp.

strong friction and aerodynamic heating.[41] As the bow shock gradually transits to the oblique shock in the downstream flow, the direction of the fluid passing through the shock gradually parallels the wall (λ gradually approaches 0), and the boundary layer gradually thickens, so the skin friction and heat flux decrease.

Another noteworthy phenomenon is that the pressure on the line of peak wall pressure increases with the displacement away from the VCO. Similar phenomena also occur for the distribution of skin friction and heat flux, as shown in Fig. 16. To study the causes of this phenomenon, we select three reference points A1, A2, and A3 above the line of peak wall pressure and streamlines s1, s2, and s3 through these three points, respectively, as shown in Fig. 17(a). It should be noted that A1, A2, and A3 are not located at the line of peak wall pressure

but are slightly higher than the wall. Figure 17(b) shows the change in density with the azimuth φ on the three streamlines. Behind the separation shock, the increase in density is slight and slow, which further indicates that the separation shock wave is relatively weak and closer to the compression wave. In the spherical coordinate system, the farther away from the VCO, the faster the increase in density, but the density growth trend on the three streamlines is similar. Although the density-increasing processes of the three streamlines from the separation to the reattachment are different, the difference in density before the reattachment line is not big, especially at $\varphi = 48°$, where the density of the three is very close. This phenomenon indicates that the reattachment and main shock wave are the main factors determining the difference in total density at different spanwise positions.
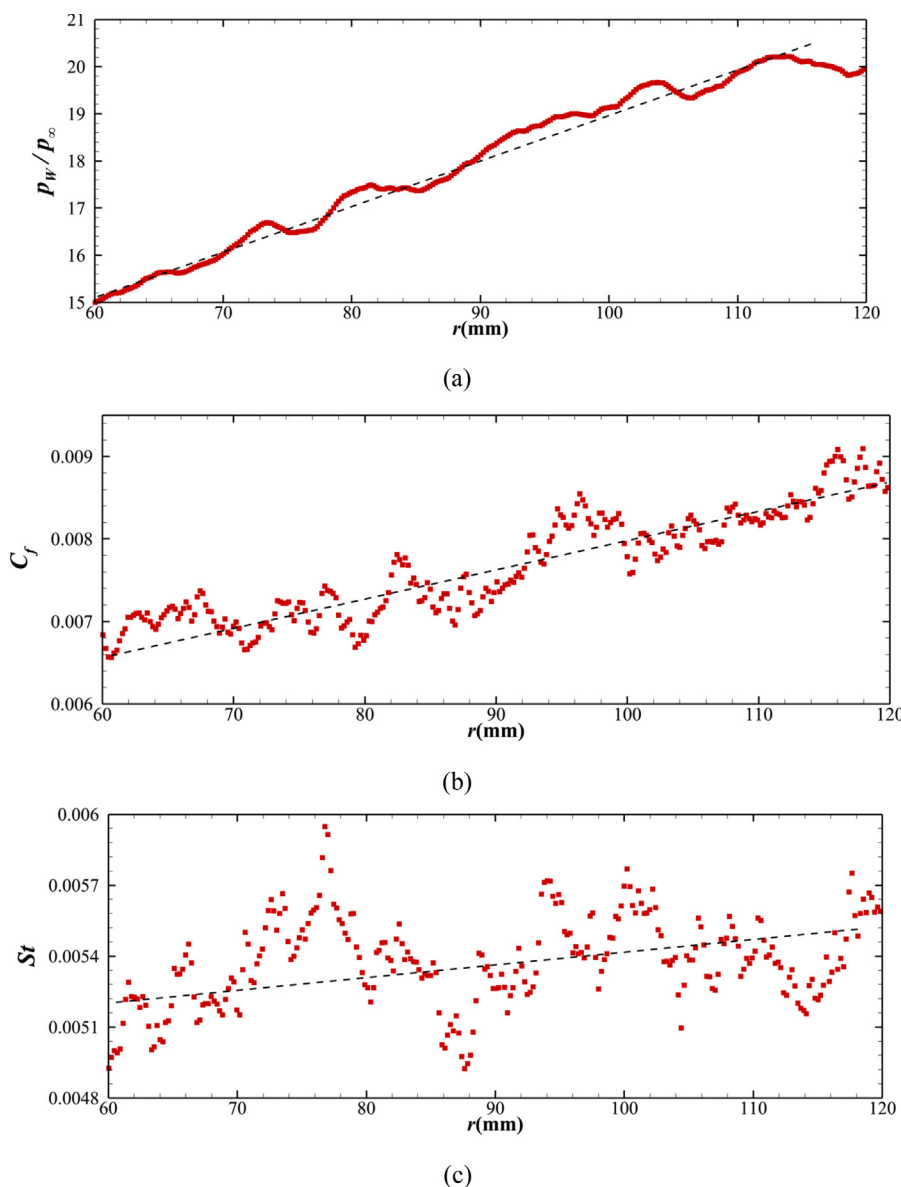
FIG. 16. Time-averaged distribution of corresponding physical quantities on the lines of peak (a) wall pressure, (b) skin friction coefficient, and (c) Stanton number. The dashed lines are the regression lines of the corresponding physical quantities.
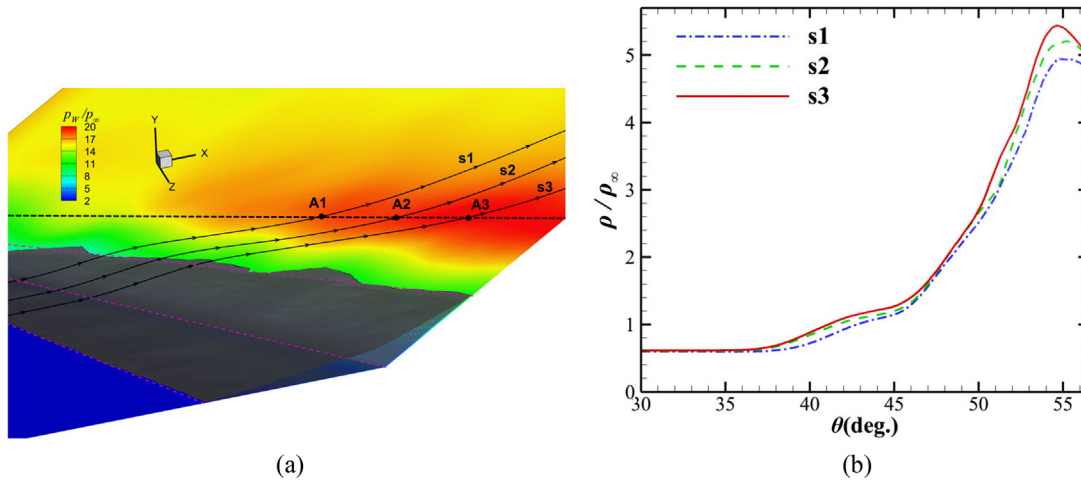
FIG. 17. (a) Three reference points A1, A2, and A3 above the line of peak wall pressure and streamlines s1, s2, and s3 passing through the three points, respectively. (b) Time-averaged distribution of density on streamlines s1, s2, and s3.

Figure 14 also shows that the density behind the main shock in the plane of $z = 45$ mm is higher than that in the plane of $z = 30$ mm. As mentioned before, the main shock angle changes with the spanwise position. Therefore, the farther away from the VCO, the stronger the shock, which leads to higher density, pressure, and temperature downstream. Nevertheless, whether there is an upper limit for such an increase in the wall pressure, skin friction, and heat flux along the r-direction needs further discussion by expanding the spanwise domain.

C. Unsteadiness

Shock wave low-frequency oscillation, a noteworthy phenomenon in STBLIs, is mainly manifested in the movement of the separation shock foot in the intermittent region at a frequency far lower than the characteristic frequency of the turbulent boundary layer. To study mid- and low-frequency effects in hypersonic 3D STBLI, we collect instantaneous wall pressure data on three planes ($z = 15$, 30, and 45 mm) after the flow reaches statistically converged results. Because the wall pressure results are virtually identical in Mesh 1 and Mesh 2, the sampling results for Mesh 1 rather than Mesh 2 are shown in the following analyses to reduce the computation cost. The Strouhal number $Sr_L = f\, U_\infty/L$ or $Sr_\delta = f\, U_\infty/\delta$ is usually used to characterize the dimensionless frequency and estimate the frequency of low-frequency oscillation, where L and δ are the length of the separation bubble and the thickness of the boundary layer, respectively. Because of the great difference in the size of the separation bubbles at the different spanwise positions, δ/U_∞ is used to normalize the time. The total time of each group of sampled data is about $1500\, \delta/U_\infty$, and the time resolution is about $0.094\, \delta/U_\infty$. The characteristic frequency of the turbulent boundary layer obtained in this case is about $3\, U_\infty/\delta$, which is higher than the outer-scale frequency U_∞/δ of general STBLI, although the two are consistent in order of magnitude. There might be insufficient evidence for the hypersonic flows to select a suitable and specific normalizer.[3] Therefore, to visually reflect the characteristic frequency in the interaction region, we use the turbulent boundary layer

characteristic frequency f_0 at E1 as the normalizer in the following analyses.

Figure 18 shows the premultiplied power spectral density (PSD) of wall pressure, where the premultiplied PSD $= f/f_0 \cdot$ PSD. There are some narrow-band peaks in Figs. 18–20, which are caused by the upstream blowing and suction disturbance. This phenomenon also exists in the study by Priebe and Martin.[42] These narrow-band peaks do not affect the analysis of other frequency motions, especially for low-frequency oscillations. In Fig. 18, there is an inconspicuous low-frequency region at the separation position, which indicates that the energy of this low-frequency motion is very low. Figure 19 compares the results for hypersonic swept and unswept[3] compression ramps at the starting position of the separation. Compared to 2D STBLI, the low-frequency energy in 3D STBLI can be negligible. This result is consistent with that of Erengil and Dolling.[14]

At present, there are two main viewpoints on the mechanism driving low-frequency oscillation: the influence of the upstream turbulent boundary layer and the intrinsic instability in the downstream separation bubble.[2] The difference in the downstream separation structure is the main cause of the opposite low-frequency characteristics in 2D and 3D interactions, as the upstream boundary layer is not very different. Because the separation shock is much weaker than reattachment and main shocks, even if there is low-frequency motion of the separation shock foot, the energy of this motion is far less than that of mid- and high-frequency motion. As the displacement from the VCO increases, the size of the separation bubble and the strength of the separation shock increase, which leads to an increase in low-frequency energy, but the energy of the low-frequency motion is still significantly weaker than that of the mid- or high-frequency motion. In addition, the mean flow of 2D interaction has no spanwise velocity in the separation region, and periodic spanwise boundary conditions are usually applied in numerical simulations, which lead to the continuous accumulation and development of perturbations in the separation region. However, the flow is not closed in the separation region of 3D interaction, so the intrinsic instability of the separated flow makes it difficult to produce a sustained effect on the separation shock wave.
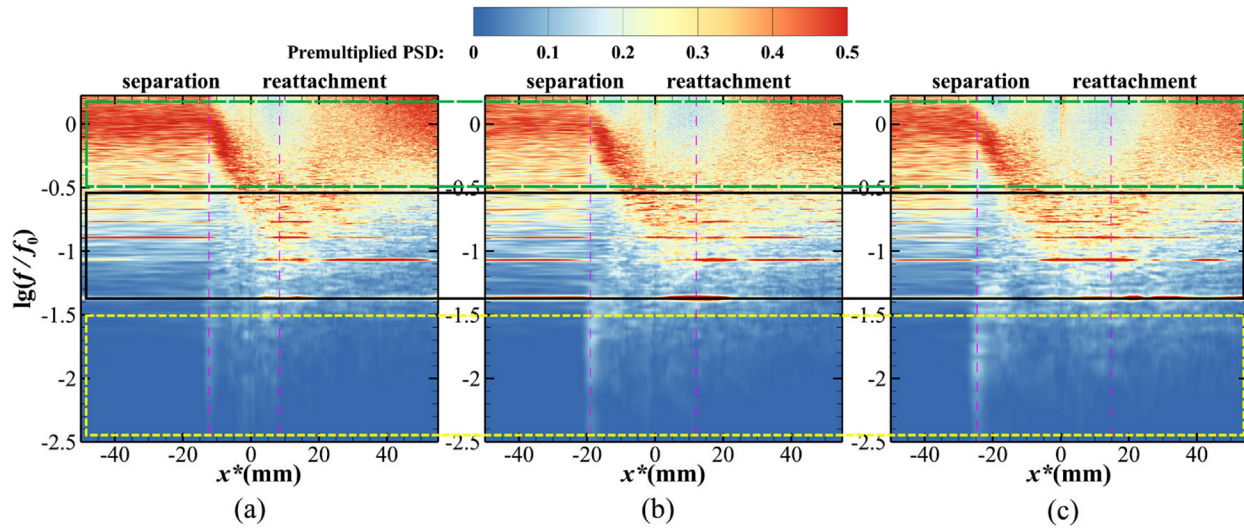
FIG. 18. Premultiplied wall-pressure PSD in the planes of (a) $z = 15$ mm, (b) $z = 30$ mm, and (c) $z = 45$ mm. The PSD is divided into the high-frequency band (green dashed line), mid-frequency band (black solid line), and low-frequency band (yellow dotted line) according to the frequency.
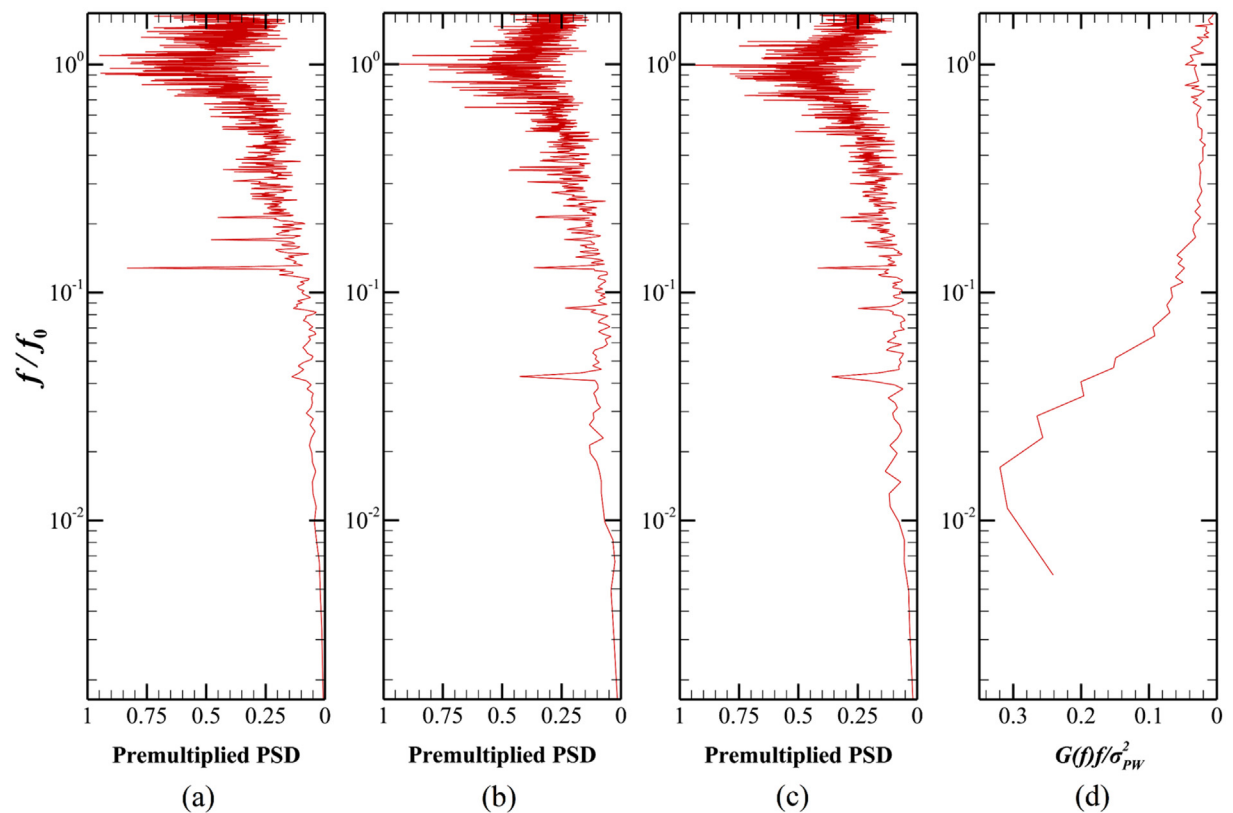
FIG. 19. Premultiplied wall-pressure PSD of separation points at different spanwise positions: (a) $z = 15$ mm, (b) $z = 30$ mm, and (c) $z = 45$ mm. (d) The wall-pressure PSD at the intermittent region in unswept compression ramps with $Ma = 5$.[3]
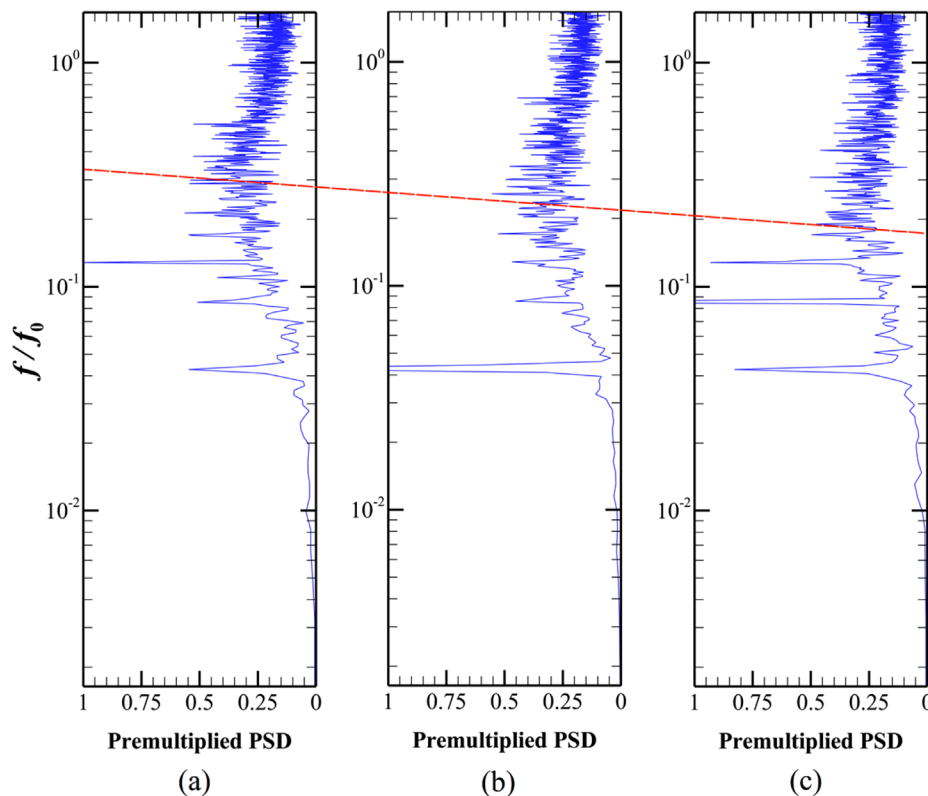
FIG. 20. Premultiplied wall pressure PSD of reattachment points at different spanwise positions: (a) $z = 15$ mm, (b) $z = 30$ mm, and (c) $z = 45$ mm. The red dashed line indicates the peak of premultiplied PSD at each position.

Adler and Gaitonde[19] believed that perturbation in the 3D interaction was difficult to maintain itself but flowed toward the boundary. In the center of the separation region, the crossflow moves along the r-direction and toward the spanwise boundary with supersonic speed. Therefore, the perturbation waves propagating at the sound speed can hardly persist in the separation region but be carried by the crossflow to the spanwise boundary. The period of the low-frequency, large-scale motion is very long, whereas it is challenging for the mid- or high-frequency pulsations to accumulate for a long time, so it is difficult for the low-frequency motion to become dominant.

Although the low-frequency instability is not obvious in the 3D STBLI, there is a notable mid-frequency instability band in the interaction region, and the characteristic frequency of the mid-frequency band is one order of magnitude lower than that of the upstream turbulent boundary layer. The mid-frequency motion is related to the shear or convective fluctuations between the outer flow and the crossflow.[19] Because the size of the crossflow region changes with the spanwise position, the length of the mid-frequency band increases along the spanwise direction. Furthermore, the spanwise change in the separation region also affects the period of the mid-frequency motion. Hence, the characteristic frequency of the mid-frequency motion decreases along the spanwise direction, as shown in Fig. 20. It can be predicted that as the spanwise computational domain increases, the characteristic frequency of the mid-frequency motion will continue to decrease. As for whether there is a cutoff frequency for the mid-frequency motion, further research is needed. It is worth mentioning that the characteristic frequency of the high-frequency motion behind the reattachment is higher than before the separation. At locations downstream of the reattachment, the flow gradually reverts to the turbulent boundary layer flow, and the thickness of the reattached boundary layer is much thinner than that of the incoming turbulent boundary layer, so the local outer scale frequency here is higher than before the separation.

IV. CONCLUSION

In this paper, we conduct a DNS of a swept compression ramp STBLI with $Ma = 6$ and unit $Re = 10\,000$/mm using the heterogeneous parallel finite difference solver OpenCFD-SCU. Based on the verification of the simulation results, the following are studied: (1) the flow structure of the hypersonic 3D STBLI, (2) the causes of peak skin friction and heat flux, and (3) the mechanism underlying the mid- and low-frequency unsteadiness.

The results show that the flow of the hypersonic swept compression ramp follows the quasi-conical symmetry, mainly manifested in linear variation in the separation region along the spanwise direction. There is a crossflow with helical motion in the separation region. The flow in the center of the crossflow is supersonic, and its velocity increases along the spanwise direction. The head of the main shock wave is a bow shock, and the farther away from the VCO, the greater the angle of the main shock.

Above the separation region, fluids from the high-energy-density region pass through the bow shock at the head of the main shock and crash into the wall behind the reattachment line, forming the peaks of skin friction and heat flux. Although the distribution of the peak friction and heating conforms to the conical self-similarity, the peak

values increase with the displacement from the VCO because of the difference in the shock wave inclination at different spanwise positions.

The low-frequency, large-scale motion near the separation shock foot is not obvious. There are two reasons for the lack of low-frequency unsteadiness: (1) compared to the reattachment shock and main shock, the separation shock wave is significantly weak; and (2) because of the supersonic crossflow, the perturbation propagating at the sound speed is difficult to maintain itself in the separation region but flows along the r-direction and toward the spanwise boundary. The mid-frequency motion is mainly caused by the shear or convective fluctuations between the outer flow and the crossflow and becomes dominant in the interaction region. Moreover, along the spanwise direction, the size of the mid-frequency region increases and its characteristic frequency decreases.

ACKNOWLEDGMENTS

AUTHOR DECLARATIONS
Conflict of Interest

The authors have no conflicts to disclose.

Author Contributions

Ji Zhang: Conceptualization (equal); Data curation (equal); Formal analysis (equal); Investigation (equal); Methodology (equal); Validation (equal); Writing – original draft (equal); Writing – review & editing (equal). **Tongbiao Guo:** Data curation (equal); Formal analysis (equal); Investigation (equal); Writing – original draft (equal); Writing – review & editing (equal). **Guanlin Dang:** Data curation (equal); Formal analysis (equal); Methodology (equal); Software (equal). **Xinliang Li:** Conceptualization (equal); Data curation (equal); Formal analysis (equal); Investigation (equal); Methodology (equal); Software (equal); Writing – review & editing (equal).

DATA AVAILABILITY

The data supporting the findings of this study are available from the corresponding author upon reasonable request.

REFERENCES

[1] D. S. Dolling, "Fifty years of shock-wave/boundary-layer interaction research: What next?," AIAA J. **39**, 1517–1531 (2001).

[2] N. T. Clemens and V. Narayanaswamy, "Low-frequency unsteadiness of shock wave/turbulent boundary layer interactions," Annu. Rev. Fluid Mech. **46**, 469–492 (2014).

[3] M. E. Erengil and D. S. Dolling, "Unsteady wave structure near separation in a Mach 5 compression ramp interaction," AIAA J. **29**, 728–735 (1991).

[4] S. Pirozzoli, F. Grasso, and T. B. Gatski, "Direct numerical simulation and analysis of a spatially evolving supersonic turbulent boundary layer at M = 2.25," Phys. Fluids **16**, 530–545 (2004).

[5] S. Pirozzoli and F. Grasso, "Direct numerical simulation of impinging shock wave/turbulent boundary layer interaction at M = 2.25," Phys. Fluids **18**, 065113 (2006).

[6] M. Wu and M. P. Martin, "Direct numerical simulation of supersonic turbulent boundary layer over a compression ramp," AIAA J. **45**, 879–889 (2007).

[7] M. P. Martin, "Direct numerical simulation of hypersonic turbulent boundary layers. I. Initialization and comparison with experiments," J. Fluid Mech. **570**, 347–364 (2007).

[8] M. Wu and M. P. Martin, "Analysis of shock motion in shockwave and turbulent boundary layer interaction using direct numerical simulation data," J. Fluid Mech. **594**, 71–83 (2007).

[9] V. Pasquariello, S. Hickel, and N. A. Adams, "Unsteady effects of strong shock-wave/boundary-layer interaction at high Reynolds number," J. Fluid Mech. **823**, 617–657 (2017).

[10] S. Priebe and M. P. Martin, "Turbulence in a hypersonic compression ramp flow," Phys. Rev. Fluids **6**, 034601 (2021).

[11] G. S. Settles and H. Y. Teng, "Cylindrical and conical flow regimes of three-dimensional shock/boundary-layer interactions," AIAA J. **22**, 194–200 (1984).

[12] G. S. Settles and F. K. Lu, "Conical similarity of shock/boundary-layer interactions generated by swept and unswept fins," AIAA J. **23**, 1021–1027 (1985).

[13] G. S. Settles and R. L. Kimmel, "Similarity of quasiconical shock wave/turbulent boundary-layer interactions," AIAA J. **24**, 47–53 (1986).

[14] M. Erengil and D. Dolling, "Effects of sweepback on unsteady separation in Mach 5 compression ramp interactions," AIAA Paper No. 1992-430, 1992.

[15] L. Vanstone, M. Saleem, S. Seckin, and N. T. Clemens, "Effect of upstream boundary layer on unsteadiness of swept-ramp shock/boundary layer interactions at Mach 2," AIAA Paper No. 2016-0076, 2016.

[16] L. Vanstone, M. N. Musta, S. Seckin, and N. Clemens, "Experimental study of the mean structure and quasi-conical scaling of a swept-compression-ramp interaction at Mach 2," J. Fluid Mech. **841**, 1–27 (2018).

[17] L. Vanstone and N. T. Clemens, "Structure and unsteadiness of swept-ramp shock wave/turbulent boundary layer interactions," in *Proceedings of the 31st International Symposium on Shock Waves 1* (Springer, Cham, 2019), pp. 81–93.

[18] M. C. Adler and D. V. Gaitonde, "Flow similarity in strong swept-shock/turbulent-boundary-layer interactions," AIAA J. **57**, 1579–1593 (2019).

[19] M. C. Adler and D. V. Gaitonde, "Dynamics of strong swept-shock/turbulent-boundary-layer interactions," J. Fluid Mech. **896**, A29 (2020).

[20] M. D. Renzo, N. Oberoi, J. Larsson, and S. Pirozzoli, "Crossflow effects on shock wave/turbulent boundary layer interactions," Theor. Comput. Fluid Dyn. **36**, 327–344 (2021).

[21] E. Elsen, P. LeGresley, and E. Darve, "Large calculation of the flow over a hypersonic vehicle using a GPU," J. Comput. Phys. **227**, 10148–10161 (2008).

[22] J. Romero, J. Crabill, J. E. Watkins, F. D. Witherden, and A. Jameson, "ZEFR: A GPU-accelerated high-order solver for compressible viscous flows using the flux reconstruction method," Comput. Phys. Commun. **250**, 107169 (2020).

[23] M. D. Renzo, L. Fu, and J. Urzay, "HTR solver: An open-source exascale-oriented task-based multi-GPU high-order code for hypersonic aerothermodynamics," Comput. Phys. Commun. **255**, 107262 (2020).

[24] M. Bernardini, D. Modesti, F. Salvadore, and S. Pirozzoli, "STREAmS: A high-fidelity accelerated solver for direct numerical simulation of compressible turbulent flows," Comput. Phys. Commun. **263**, 107906 (2021).

[25] X. L. Li, D. X. Fu, Y. W. Ma, and X. Liang, "Direct numerical simulation of shock/turbulent boundary layer interaction in a supersonic compression ramp," Sci. China Phys. Mech. Astron. **53**, 1651–1658 (2010).

[26] F. Tong, X. Li, Y. Duan, and C. Yu, "Direct numerical simulation of supersonic turbulent boundary layer subjected to a curved compression ramp," Phys. Fluids **29**, 125101 (2017).

[27] X. K. Zhu, C. P. Yu, F. L. Tong, and X. L. Li, "Numerical study on wall temperature effects on shock wave/turbulent boundary-layer interaction," AIAA J. **55**, 131–140 (2017).

[28] J. Y. Duan, X. Li, X. L. Li, and H. W. Liu, "Direct numerical simulation of a supersonic turbulent boundary layer over a compression–decompression corner," Phys. Fluids **33**, 065111 (2021).

[29] T. Guo, J. Fang, J. Zhang, and X. Li, "Direct numerical simulation of shock-wave/boundary layer interaction controlled with convergent–divergent riblets," Phys. Fluids **34**, 086101 (2022).

[30] O. C. Zienkiewicz and R. Codina, "A general algorithm for compressible and incompressible flow. I. The split, characteristic-based scheme," Int. J. Numer. Methods Fluids **20**, 869–885 (1995).

[31] X. L. Li, Y. Leng, and Z. W. He, "Optimized sixth-order monotonicity-preserving scheme by nonlinear spectral analysis," Int. J. Numer. Methods Fluids **73**, 560–577 (2013).

[32] G. S. Jiang and C. W. Shu, "Efficient implementation of weighted ENO schemes," J. Comput. Phys. **126**, 202–228 (1996).

[33] L. Duan, I. Beekman, and M. P. Martin, "Direct numerical simulation of hypersonic turbulent boundary layers. II. Effect of wall temperature," J. Fluid Mech. **655**, 419–445 (2010).

[34] S. Pirozzoli and M. Bernardini, "Turbulence in supersonic boundary layers at moderate Reynolds number," J. Fluid Mech. **688**, 120–168 (2011).

[35] M. Elena and J. P. Lacharme, "Experimental study of a supersonic turbulent boundary layer using a laser Doppler anemometer," J. Mec. Theor. Appl. **7**, 175–190 (1988). https://www.scopus.com/inward/record.uri?eid=2-s2.0-0023862848&partnerID=40&md5=a339de1c82ab0a2d66a795a48c78258a

[36] S. Piponniau, J. P. Dussauge, J. F. Debiève, and P. Dupont, "A simple model for low-frequency unsteadiness in shock-induced separation," J. Fluid Mech. **629**, 87–108 (2009).

[37] P. R. Spalart, "Direct simulation of a turbulent boundary layer up to $R_\theta = 1410$," J. Fluid Mech. **187**, 61–98 (1988).

[38] L. P. Erm and P. N. Joubert, "Low-Reynolds-number turbulent boundary layers," J. Fluid Mech. **230**, 1–44 (1991).

[39] R. Legendre, "Lignes de courant d'un écoulement permanent, décollement et séparation," La Recherche Aérospatiale No. 1977-6, 1977.

[40] J. Jeong and F. Hussain, "On the identification of a vortex," J. Fluid Mech. **285**, 69–94 (1995).

[41] J. D. Anderson, *Hypersonic and High Temperature Gas Dynamics*, 2nd ed. (McGraw-Hill Book Company, New York, 2006), pp. 396–398.

[42] S. Priebe and M. P. Martin, "Low-frequency unsteadiness in shock wave–turbulent boundary layer interaction," J. Fluid Mech. **699**, 1–49 (2012).

[43] G. Dang, S. Liu, T. Guo, J. Duan, and X. Li, "Direct numerical simulation of compressible turbulence accelerated by graphics processing unit. Part 1: An open-source high accuracy accelerated computational fluid dynamic software," (2022). arXiv:2209.15333.